Dipole phase and photoelectron group delay in inner-shell photoionization

A. S. Kheifets*
Research School of Physics and Engineering, The Australian National University, Canberra, Australian Capital Territory 0200, Australia

S. Saha and P. C. Deshmukh
Department of Physics, Indian Institute of Technology Madras, Chennai 600036, India

D. A. Keating and S. T. Manson
Department of Physics and Astronomy, Georgia State University, Atlanta, Georgia 30303, USA
(Received 2 October 2015; published 28 December 2015)

We conduct a systematic study of the dipole phase and the photoelectron group delay (Wigner time delay) in inner shell photoionization of noble gas atoms from Ne to Xe. Our study encompasses the tender x-ray spectral range and extends to 1 keV photoelectron energy. We employ both the relativistic and the nonrelativistic versions of the random-phase approximation with exchange. We identify the long-range Coulomb and short-range Hartree-Fock contributions to the dipole phase which governs the Wigner time delay variation from the threshold to the whole considered range of photoelectron energies.

DOI: 10.1103/PhysRevA.92.063422 PACS number(s): 32.80.Aa, 32.80.Fb, 32.80.Zb, 42.50.Hz

I. INTRODUCTION

Perfect or complete scattering experiments enable a deep insight into the collision mechanisms and provide a stringent test of theory [1]. This is particularly true for photoionization where a complete experiment can be realized by simultaneous measurements of photoelectron angular distributions and spin-polarization parameters [2]. In such a complete experiment, the photoionization amplitudes and their relative phases can be obtained experimentally and compared with *ab initio* calculations [3].

Recent advances in ultrashort laser generation techniques have given an alternative experimental access to the dipole photoionization phase. The availability of the phase-locked XUV pump and IR probe laser pulses has allowed for an accurate determination of the phase of the dipole photoionization amplitude and the photoelectron group delay. In the attosecond streaking technique, an isolated XUV pump pulse is superimposed with a phase-locked IR probe to convert the relative XUV-IR phase into the kinetic energy of the photoelectron [4]. This conversion is used to obtain the timing of the photoelectron wave packet release [5]. The latter can be interpreted in terms of the photoelectron group delay (also known as the Wigner time delay or the Wigner-Eisenbud-Smith time delay [6–8]). An alternative RABBITT (reconstruct the attosecond beatings caused by interference of two-photon transitions) technique employs an attosecond pulse train as a pump superimposed with a spectrally narrow IR probe to reconstruct the attosecond beatings caused by interference of two-photon transitions [9]. The phase of these beatings encodes the dipole photoionization phase which again can be converted to the Wigner time delay [10,11]. Yet another alternative method to reconstruct the photoionization phase is the high-harmonic generation (HHG) technique. Because photorecombination is the inverse process to photoionization, their phases are identical. The photorecombination phase is encoded in the spectral phase of the harmonic comb and can be retrieved using the RABBITT technique [12] or harmonic spectroscopy based on two-color driving pulses [13].

So far, these phase retrieval techniques have been exploited in the XUV spectral range not significantly exceeding the photon energy of 100 eV. However, recent experiments with mid-IR driving pulses have allowed the extension of the harmonic emission to much higher photon energies [14,15]. This extension allows the study of photoemission processes in inner atomic shells and the retrieval of the phase and timing information. At the same time, accurate modeling of the HHG process in this spectral range requires knowledge of the photorecombination phase [16].

A parallel development, which potentially allows the study of the photoionization phase over an extended spectral range, is the streaking of a free-electron laser (FEL) radiation with a THz probe [17,18]. The same idea of the THz streak camera allows for a high-precision measurement of the arrival time of a FEL pulse [19–21]. The photoionization time delay is also needed for understanding the energy spectra of the photoelectrons created by the FEL pulses [22]. These spectra do not exactly mimic the spectrum of the photon pulse, rather they have contributions from the photon pulse spectrum and the emission spectrum corresponding to the ionization time. Depending on the ionization time and the temporal structure of the FEL pulse, the spectrum of the electrons can be dominated by one of these components.

To address these needs, we conduct a systematic study of the dipole photoionization phase and the Wigner time delay in inner shells of the noble gas atoms from Ne to Xe. This study encompasses the tender x-ray spectral range and extends to 1 keV photoelectron energy. This includes the K and L shells of Ne; the K, L, and M shells of Ar; and the L and M shells of Kr and Xe (see Table I for respective binding energies). The present study partially overlaps with, and is complementary to, our previous work [24] where time delay in valence shell photoionization of noble gases was investigated.

Our methodology (Sec. II) is similar to that of the previous works [24,25] and employs both nonrelativistic and relativistic

*A.Kheifets@anu.edu.au

TABLE I. Electron binding energies, in electron volts, as collated in the *X-Ray Data Booklet* [23].

	K $1s$	LI $2s$	LII $2p_{1/2}$	LIII $2p_{3/2}$	MI $3s$	MII $3p_{1/2}$	MIII $3p_{3/2}$	MIV $3d_{3/2}$	MV $3d_{5/2}$
Ne	870.2	48.5	21.7	21.6					
Ar	3206	326.3	250.6	248.4	29.3	15.9	15.7		
Kr	14 326	1921	1731	1678	292.8	222.2	214.4	95.0	93.8
Xe	34 561	5453	5107	4786	1149	1002	940.6	689.0	676.4

versions of the random phase approximation with exchange (RPAE and RRPA, respectively). As a test of accuracy, we compare our calculated subshell photoionization cross sections with the experimental values collated by Berkowitz [26] for Ne, Ar, and Kr and calculated by Band *et al.* [27] for Xe (Sec. III A). Satisfied with these tests, we proceed with the photoionization phase calculation (Sec. III B). We compare the phase results from correlated RPAE calculations with those from the single-electron Hartree-Fock (HF) approximation. Thus we can identify clearly the effect of many-electron correlation. Then we convert the phase into the Wigner time delay calculated in the direction of the polarization of the XUV radiation (Sec. III C). We do not evaluate the corrections induced by the coupling of the long-range Coulomb ionic potential and the streaking field (CLC corrections). These corrections are of universal nature and can be found in the literature [28,29]. Finally, we elucidate the role of relativistic effects by making a comparison of the time delay results from the RPAE and RRPA calculations (Sec. III D)

II. THEORETICAL METHOD AND COMPUTATION DETAILS

For the nonrelativistic RPAE, we follow closely the photoionization formalism as outlined in our previous work [24]; the relativistic RRPA development is essentially the same, but based on the Dirac equation rather than the Schrödinger equation [25]. Here we reproduce only a few essential details to benefit the reader. We evaluate the single-photon dipole matrix element $\langle\psi_{\boldsymbol{k}}^{(-)}|\hat{z}|\phi_i\rangle$ from a bound state $\phi_i(\boldsymbol{r}) = Y_{l_i m_i}(\hat{\boldsymbol{r}})R_{n_i l_i}(r)$ to an incoming scattering state with the given photoelectron momentum $\boldsymbol{k}$:

$$\psi_{\boldsymbol{k}}^{(-)}(\boldsymbol{r}) = \frac{(2\pi)^{3/2}}{k^{1/2}} \sum_{lm} i^l e^{-i\delta_l(E)} Y_{lm}^*(\hat{\boldsymbol{k}}) Y_{lm}(\hat{\boldsymbol{r}}) R_{kl}(r). \quad (1)$$

We conduct the spherical integration to arrive at the following expression:

$$\langle\psi_{\boldsymbol{k}}^{(-)}|\hat{z}|\phi_i\rangle = \frac{(2\pi)^{3/2}}{k^{1/2}} \sum_{\substack{l=l_i\pm1 \\ m=m_i}} e^{i\delta_l(E)} i^{-l} Y_{lm}(\hat{\boldsymbol{k}}) \times \begin{pmatrix} l & 1 & l_i \\ m & 0 & m_i \end{pmatrix} \langle kl \| \hat{D} \| n_i l_i \rangle. \quad (2)$$

Here $\langle kl \| \hat{D} \| n_i l_i \rangle$ is the reduced dipole matrix element, stripped of all the angular momentum projections. The partial photoionization cross section for the transition from the occupied state $n_i l_i$ to the photoelectron continuum state kl is calculated as

$$\sigma_{n_i l_i \to kl}(\omega) = \tfrac{4}{3}\pi^2 \alpha a_0^2 \omega |\langle kl \| \hat{D} \| n_i l_i \rangle|^2, \quad (3)$$

with ω being the photon energy, α the fine structure constant, and a_0 the Bohr radius. The atomic units $e = m = \hbar = 1$ are used in this expression and throughout the paper.

In the independent electron HF approximation, the reduced dipole matrix element is evaluated as a radial integral:

$$\langle kl \| \hat{D} \| n_i l_i \rangle = [l][l_i] \begin{pmatrix} l & 1 & l_i \\ 0 & 0 & 0 \end{pmatrix} \int r^2 dr R_{kl}(r) r R_{n_i l_i}(r), \quad (4)$$

where the notaion $[l] = \sqrt{2l+1}$ is used. The basis of the occupied atomic states $\|n_i l_i\rangle$ is defined by the self-consistent HF method and calculated using the computer code [30]. The continuum electron orbitals $\langle kl\|$ are defined within the frozen-core HF approximation and evaluated using the computer code [31].

In the RPAE, the reduced dipole matrix element is found by summing an infinite sequence of Coulomb interactions between the photoelectron and the hole in the ionized shell. This leads to a system of integral equations which can be represented graphically by the diagrams of Fig. 1. Figure 1(a) represents the sum of all Coulomb interactions, Fig. 1(b) depicts the HF term given by Eq. (4), and Figs. 1(c)–1(f) represent RPAE corrections. Figures 1(c) and 1(d) are known as time direct (foreward), and Figs. 1(e) and 1(f) are known as time reverse (backward). Figures 1(d) and 1(f) account for

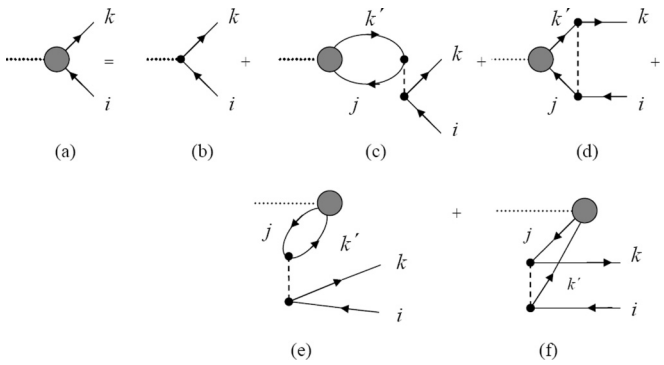

FIG. 1. Diagramatic representation of the photoionization amplitude $\langle kl|\hat{D}|n_i l_i\rangle$ in the RPAE. Here, the time axis is directed from left to right, the lines with arrows to the left (right) correspond to holes (electrons) in a filled atomic shell, a dotted line represents an incoming photon, a dashed line represents the Coulomb interaction between charged particles, and a shaded circle marks the effective operator $\hat{D}$ for the photon-atom interaction, which accounts for electron correlation in the atom.

the exchange interaction in the atom, and thus are called the exchange diagrams. As is seen from Fig. 1, a virtual excitation in the shell j to the ionized electron state $\boldsymbol{k}'$ may affect the final ionization channel from the shell i. This way the RPAE accounts for the effect of the intershell $i \leftrightarrow j$ correlation, also known as interchannel coupling. It is important to note that, within the RPAE framework, the reduced dipole matrix element is complex and, thereby, adds to the phase of the dipole amplitude.

The photoelectron group delay, which is the energy derivative of the phase of the complex photoionization amplitude, is evaluated as

$$\tau = \frac{d}{dE} \arg f(E) \equiv \mathrm{Im}[f'(E)/f(E)]. \tag{5}$$

Here $f(E)$ is used as a shortcut for the amplitude $\langle \psi_{\boldsymbol{k}}^{(-)} | \hat{z} | \phi_i \rangle$ given by Eq. (2) and evaluated for $E = k^2/2$ and $\hat{\boldsymbol{k}} \parallel z$.

In the RRPA, we use the following expression for the photoionization amplitude [32]:

$$T_{JM}^{(\lambda)} \propto \sum_{\bar{\kappa}\bar{m}} [\chi_\nu^\dagger \Omega_{\bar{\kappa}\bar{m}}(\hat{\boldsymbol{k}})](-1)^{\bar{j}-\bar{m}} \begin{pmatrix} \bar{j} & J & j \\ -\bar{m} & M & m \end{pmatrix} \times i^{1-\bar{l}} e^{i\delta_{\bar{\kappa}}} \langle \bar{a} \| Q_J^{(\lambda)} \| a \rangle . \tag{6}$$

Here $\lambda = J = 1$ and $M = 0$ for the dipole electric transition with the light which is linearly polarized in the z direction. The reduced matrix element is expressed as

$$\langle \bar{a} \| Q_J^{(\lambda)} \| a \rangle = (-1)^{j+1/2} [\bar{j}][j] \begin{pmatrix} j & \bar{j} & J \\ -1/2 & 1/2 & 0 \end{pmatrix} \times \pi(\bar{l}, l, J - \lambda + 1)\, R_J^{(\lambda)}(\bar{a}, a). \tag{7}$$

Here π is parity and the radial integral $R_J^{(\lambda)}(\bar{a},a)$ is calculated between the initial state $a = (n\kappa)$ and the final (energy scale normalized) state $\bar{a} = (E,\bar{\kappa})$. The variables n, κ, and m are principal and angular momentum quantum numbers; $\kappa = \mp(j + 1/2)$ for $j = l \pm 1/2$, where j and l are the total and orbital angular momenta. The spherical spinor is given in terms of spherical harmonics and two-component Pauli spinors:

$$\Omega_{\kappa m}(\hat{\boldsymbol{n}}) = \sum_{\lambda=\pm 1/2} C_{l\,(m-\lambda),1/2\,\lambda}^{jm} Y_{l\,(m-\lambda)}(\hat{\boldsymbol{n}}) \chi_\lambda . \tag{8}$$

The amplitude Eq. (6) is evaluated in the polarization z direction and fed into Eq. (5) to calculate the time delay.

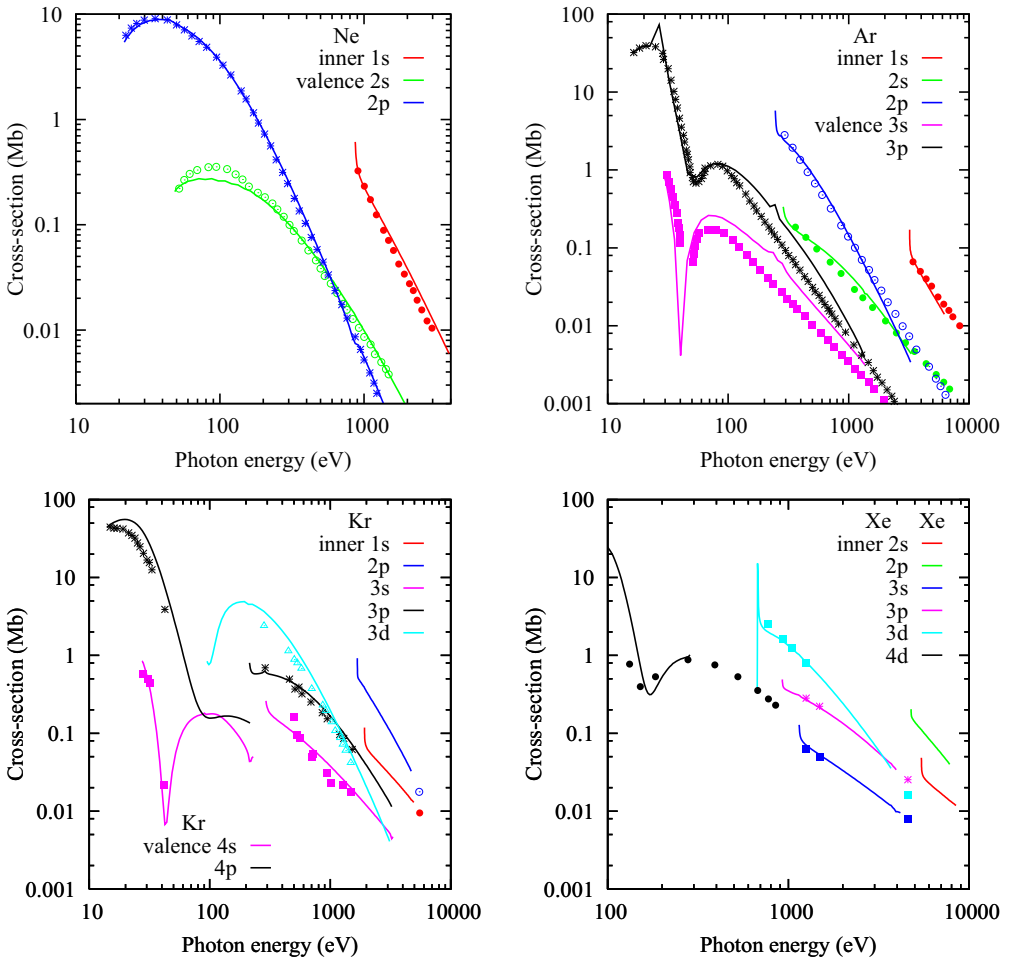

FIG. 2. (Color online) Shell photoionization cross sections of Ne, Ar, Kr, and Xe from nonrelativistic RPAE calculations are shown with lines. Similarly colored dots represent the literature values collated by Berkowitz [26] for Ne, Ar, and Kr and calculated by Band *et al.* [27] for Xe.

III. RESULTS AND DISCUSSION

A. Shell photoionization cross sections

The partial (subshell) photoionization cross sections from the RPAE calculations are displayed in Fig. 2 for Ne and Ar (top) and Kr and Xe (bottom). The present calculated results are compared with experimental values collated by Berkowitz [26] for Ne, Ar, and Kr and calculated by Band *et al.* [27] for Xe. Agreement with the literature data is good for inner shells but some deviation is visible for the valence shells. This deviation may be due to interchannel correlations that are not accounted for by the RPAE, e.g., interchannel coupling with ionization-plus-excitation channels. The inner shells are tightly bound by the nucleus and their electron states are well described by the independent electron HF approximation. Note further, that our RRPA results (not shown) are essentially identical to the RPAE results on the scale shown in Fig. 2.

B. Phase analysis

The phases of the dipole photoionization amplitudes $\arg f(E)$, as calculated in the RPAE, are displayed in Fig. 3 for Ne and Ar (top) and Kr and Xe (bottom). To demonstrate the effect of correlation, primarily in the form of interchannel coupling, the RPAE phases are compared with the HF results. For better visual comparison, the long-range Coulomb phase is subtracted from both the RPAE and the HF results. At the HF level, the reduced matrix element, Eq. (4), is real and thus the phase of the complex dipole matrix element, Eq. (2), is defined by the scattering phases $\delta_{l_i\pm1}(E)$. According to Fano's propensity rule [33], the dipole transition with the increased momentum $l = l_i + 1$ is usually dominant. In such a situation, $\arg f(E) \simeq \delta_{l_i+1}(E)$. It is this phase, from which the Coulomb long-range phase is subtracted, that is labeled as HF in the legend of Fig. 3.

The scattering potential acting upon the photoelectron is the sum of the Coulomb field of the nucleus and the HF potential of the frozen electron core of the residual ion. So the photoelectron scattering phase $\delta_l(E)$ contains both the long-range Coulomb and the short-range Hartree-Fock components. The Coulomb phase is given by the expression $\sigma_l(E) = \arg\Gamma(1 + l + i\eta)$, where the Sommerfeld parameter $\eta = -Z/\sqrt{2E}$ is determined by the final-state ionic charge; for photoionization of neutral atoms, $Z \equiv 1$. The Coulomb phase at small photoelectron energy diverges [34]:

$$\sigma_l(E) \simeq \eta[\ln\sqrt{(l+1)^2+\eta^2} - 1] \to \eta \ln|\eta|. \qquad (9)$$

The phase shift due to the short-range potential, i.e., the difference of the total phase and the Coulomb phase, is related to the asymptotic quantum defect μ_∞ according to the Levinson-Seaton theorem $\delta_L(E \to 0) - \sigma_L(E \to 0) = \mu_\infty\pi$ [35], where E is the photoelectron energy.

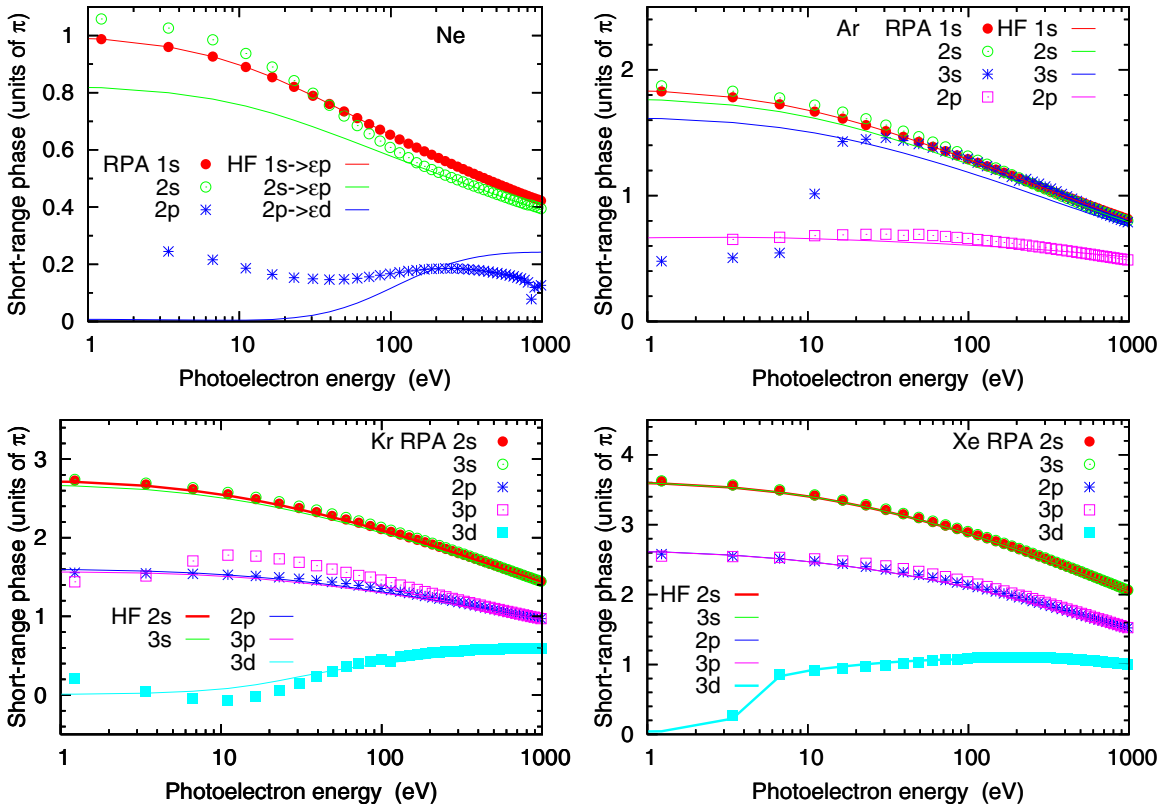

FIG. 3. (Color online) Phases of the photoionization amplitude in various shells of Ne, Ar, Kr, and Xe from nonrelativistic RPAE calculations are shown with dots. Similarly colored solid lines represent the HF scattering phase in the corresponding dominant photoionization channel. The corresponding Coulomb phases are subtracted from both the RPAE and the HF results. So only the short-range contributions to the phases are plotted.

TABLE II. Quantum defect parameters from the discrete binding energy fit $E_{n_i\underline{l_i}nl} = -Z_{\rm eff}^2/(n-\mu)^2$, with $Z_{\rm eff} = 1$ compared with the logarithmic phase interpolation to the 1 eV photoelectron kinetic energy for various Rydberg series. The hole state nl is underlined in the table captions.

	Neon			Argon				Krypton					Xenon				
$n_i\underline{l_i}nl$	$1\underline{s}np$	$2\underline{s}np$	$2\underline{p}nd$	$1\underline{s}np$	$2\underline{s}np$	$3\underline{s}np$	$2\underline{p}nd$	$2\underline{s}np$	$3\underline{s}np$	$2\underline{p}nd$	$3\underline{p}nd$	$3\underline{d}nf$	$2\underline{s}np$	$3\underline{s}np$	$2\underline{p}nd$	$3\underline{p}nd$	$3\underline{d}nf$
N_l	1	1	0	2	2	2	0	3	3	1	1	0	4	4	2	2	0
μ	1.07	0.85	0.011	1.97	1.86	1.67	0.53	2.84	2.76	1.58	1.51	0.004	3.77	3.72	2.90	2.90	0.006
Δ	0.99	0.82	0.01	1.84	1.77	1.62	0.66	2.72	2.67	1.60	1.57	0.02	3.61	3.61	2.62	2.62	0.0

The asymptotic quantum defects μ_∞ are obtained for the various $n_i\underline{l_i}nl$ Rydberg series using the following expression:

$$E_{n_i\underline{l_i}nl} = -\frac{Z^2}{(n-\mu_\infty)^2},\ Z=1,\ n\to\infty.$$

Here $E_{n_i\underline{l_i}nl}$ is the energy of the state $(n_il_i)^{-1}nl$ (in Rydbergs) with respect to the $(n_il_i)^{-1}$ threshold of the ion; the results are shown in Table II. When analyzing these results, one should bear in mind that, for a neutral target, the scattering phase at zero energy is related to the number of the bound target states of angular momentum l, N_l, by the Levinson's theorem, $\delta_l(k\to 0) = N_l\pi$. Looking at Table II, we see indeed that for lighter atoms generally $\mu \sim N_l$. For instance, in the ionic core of Ne^+, there is one occupied $2p$ orbital and no nd orbitals. Hence the short-range phase tends to one unit of π for $1s$ and $2s$ shell photoionization and to zero for $2p$ photoionization. As the number of occupied shells grows from Ne to Xe, the same increase in the μ parameters can be seen in the table. In addition, in Kr and Xe the number of occupied d shells is mismatched by one unit from the quantum defect. This reinforces the idea that Levinson's theorem applies only very approximately to positive ions.

In Table II, we also show the HF phase difference with the Coulomb phase in the dominant photoionization channel near the threshold:

$$\Delta = \frac{1}{\pi}[\delta_{\ell_i+1}(\epsilon) - \sigma_{\ell_i+1}(\epsilon)]_{\epsilon\to 0}.$$

Thus defined phase difference Δ may be compared with the quantum defect parameter μ. This comparison made in Table II shows a close correspondence between the two parameters μ and Δ for the various np series and for some of the nd series; these are the channels where the short-range HF phase is monotone decreasing from the threshold [36]. In the other nd channels, along with the nf channel, there are significant shape resonances in the threshold region so the extrapolation is less accurate.

Comparison of the short-range RPAE and HF phases in Fig. 3 shows that for the inner shells, especially in heavier

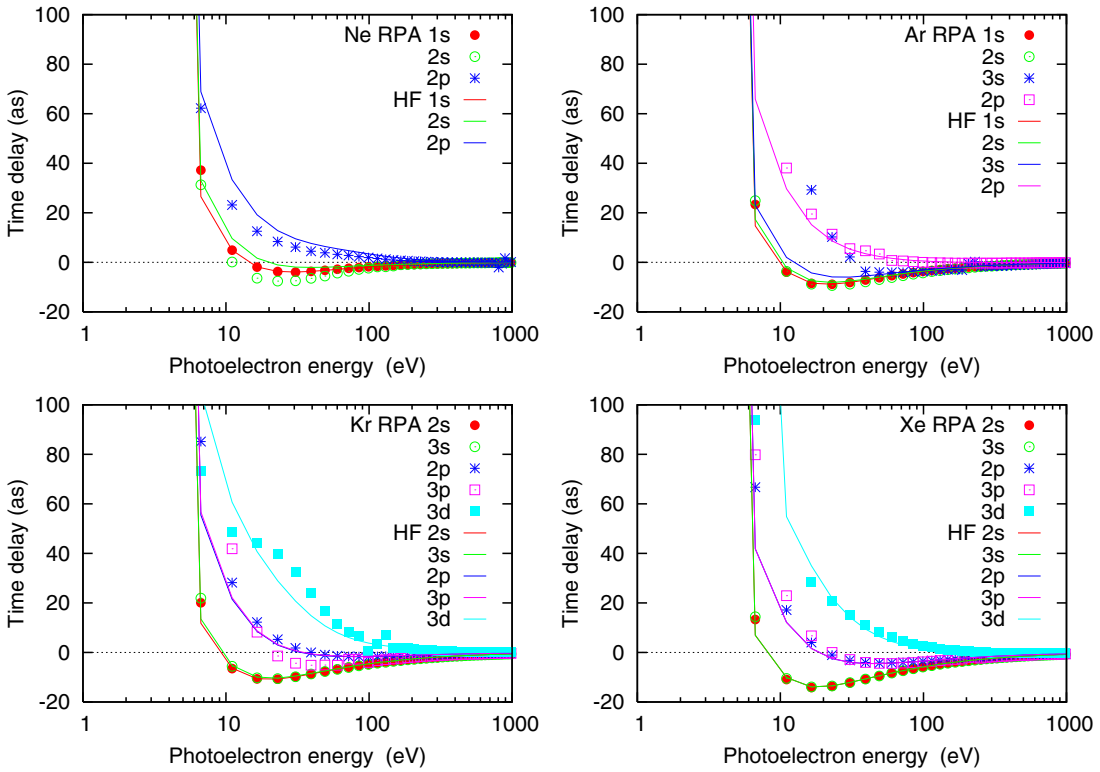

FIG. 4. (Color online) Photoelectron group delays (Wigner time delays) in various shells of Ne, Ar, Kr, and Xe from nonrelativistic RPAE calculations are shown with dots. Similarly colored solid lines represent the analogous HF results summed over all the photoionization channels.

atoms, these two calculations produce very similar results. This means that the role of the correlation is limited for the inner-shell photoionization processes. Indeed, the inner-shell electrons are tightly bound by the nuclear Coulomb potential and their interaction with the neighboring subshells is generally relatively weak. In Ne, the innermost $1s$ phase does not show any visible difference between the RPAE and HF phases. The deviation is quite visible however, for the valence $2s$ and $2p$ shells. In Ar, all the HF and RPAE phases are rather close except for the $3s$ shell, which demonstrates a very strong deviation due to profound correlation with the outer $3p$ shell. This result is acknowledged in our previous work [24]. In Kr, the inner $2s$, $2p$, and $3s$ phases are well described by the HF model while the intermediate $3p$ and $3d$ electrons show noticeable deviation of the HF from the RPAE results. In Xe, all the phases shown are HF-like because we only studied the innermost shells.

Note that, in all cases shown, the phases exhibit a monotone increase from threshold at the lower energies, owing to the dominance of the Coulomb phase near threshold. At the higher energies, as mentioned above, the Coulomb phase rapidly approaches zero, so the behavior of the total phase is dominated by the phase generated by the short-range potential. For the $ns \to \epsilon p$ channels this phase is monotone decreasing, and this leads to the situation seen in Fig. 3 where the total phases in the $ns \to \epsilon p$ channels increase rapidly from threshold, reach a maximum, and then decrease monotonically towards zero, with increasing energy. The $np \to \epsilon d$ channels, on the other hand, do not all behave in the same manner. For Ne and Ar, the short-range d-wave phase never reaches an appreciable value, so the turnover of the total phase occurs at a rather large value of the energy, larger than is displayed in Fig. 3. For Kr and Xe, on the other hand, there are shape resonances in the $np \to \epsilon d$ channels [36,37] so the short-range phases do reach appreciable values; as a result, the behavior of the total phases is just like that of the $ns \to \epsilon p$ channels. And for the $3d \to \epsilon f$ channels, the turnovers again are well beyond the plotted values.

C. Time delay

Photoelectron group delays (Wigner time delays) in various shells of Ne and Ar (top) and Kr and Xe (bottom) are shown in Fig. 4. The typical behavior of the group delay can be understood from the phase analysis of the previous section. The Coulomb singularity, Eq. (9), drives the phase to large negative values as the photoelectron energy decreases near the threshold. Hence the Wigner time delay becomes very large and positive $\tau_W \propto E^{-3/2} \ln(1/E)$ as can be seen by taking the derivative of Eq. (9) with respect to E. We note that the same energy dependence is carried by the CLC corrections $\tau_{\rm CLC} \propto E^{-3/2} \ln(aE + b)$ [28,38,39] but these corrections are *negative*. This results in the large and negative net atomic time delay $\tau_a = \tau_W + \tau_{\rm CLC}$ when the time delay measurement is taken very close to the threshold. However, the Wigner component τ_W cannot be entirely neglected when analyzing the near-threshold time delay measurement results as in Ref. [18].

At modest photoelectron energies, the phase bends over as it becomes influenced by the short-range HF component. Somewhere near this point, the time delay changes its sign and becomes negative. The exception is the np shells in Ne and Ar and the nd shells in Kr and Xe where the photoelectrons in the dominant $l_i + 1$ photoionization channel do not have bound states with matching orbital character in the ionized core. At large photoelectron energies, the time delay gradually goes to zero because the long-range Coulomb contribution to the phase becomes vanishingly small and the short-range HF contribution approaches zero extremely slowly, so slowly that its derivative also becomes vanishingly small.

The deviation of the HF and RPAE phases is exemplified in the time delay plots. It is most clearly visible in the valence shells of Ne and Ar, along with the $3d$ subshell of Kr. In all cases, however, the HF and RPAE time delays are qualitatively similar. To summarize, the low (kinetic)-energy time delay is dominated by the Coulomb phase. The high-energy region

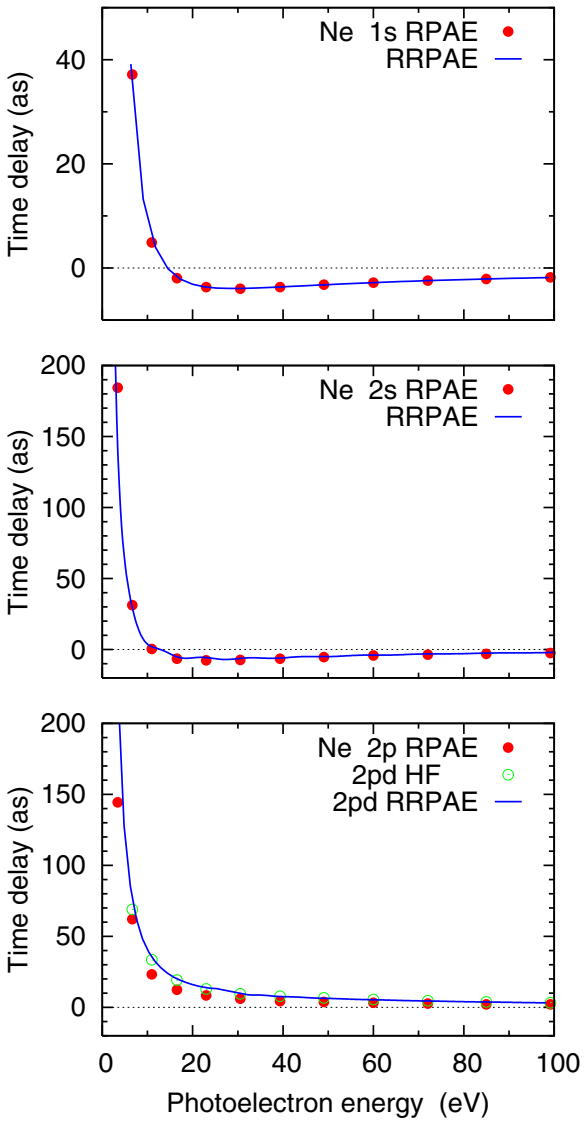

FIG. 5. (Color online) Time delay in photoionization of the $1s$, $2s$, and $2p$ shells of Ne. Nonrelativistic RPAE results (red solid circles) are compared with RRPA results (blue solid lines) for $1s \to \epsilon p$, $2s \to \epsilon p$, and $2p \to \epsilon d$ ionization channels. The HF calculation for the $2p \to \epsilon d$ ionization channel is shown by the (green) open circles.

seems to be dominated by the short-range HF phase; correlation in the form of interchannel coupling becomes relatively unimportant at high energy (except possibly near inner-shell thresholds). Thus, correlation plays no role in the qualitative behavior of the time delay vs energy, but it can affect the quantitative behavior.

D. Comparison of RPAE and RRPA calculations

To elucidate the role of relativistic effects in time delay calculations, we compare the RPAE and RRPA results. These comparisons for Ne, Kr, and Xe are shown in Figs. 5–7, respectively.

Non surprisingly, for such a light atom as Ne, there is no visible deviation between the RPAE and RRPA results in the $1s$ and $2s$ ionizations. However, a deviation can be detected in the $2p$ shell ionization. This is largely because the RPAE calculation includes the sum of the two photoionization channels $2p \to \epsilon d$ and $2p \to \epsilon s$, whereas the RRPA result includes only the stronger $2p \to \epsilon d$ channel. To match this calculation, we make a comparison with the analogous HF result and agreement is much improved.

A similar comparison for Kr and Xe is made in Figs. 6 and 7, respectively. Even though, these atoms are significantly heavier than Ne, relativistic effects do not show up in the time delay of the $2s$ shell and both the RPAE and the RRPA results practically coincide. The difference between the two calculations for the $2p$ shell can again be attributed to the partial summation of the photoionization channels. When only the $2p \to \epsilon d$ channel is included in the HF calculation, it becomes very close to the analogous RRPA result.

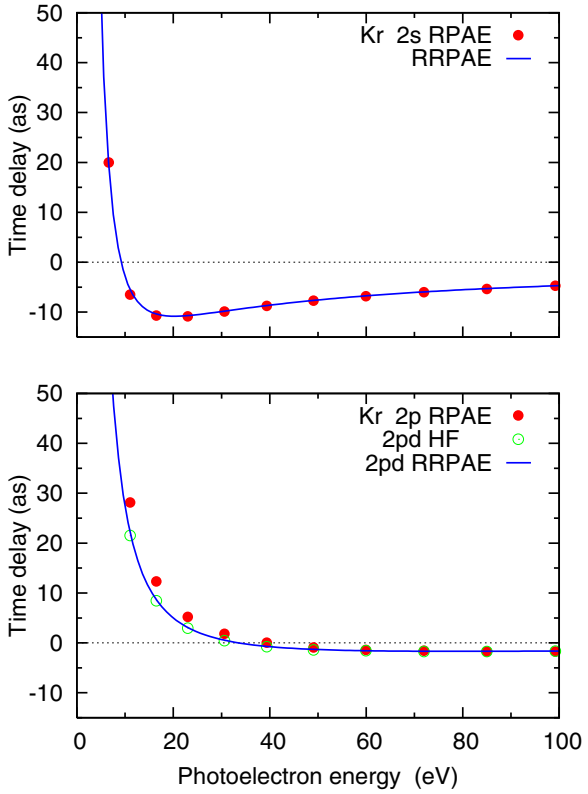

FIG. 6. (Color online) Time delay in photoionization of the $2s$ and $2p$ shells of Kr. Nonrelativistic RPAE results (red filled circles) are compared with RRPA results (blue solid lines) for $2s \to \epsilon p$ and $2p \to \epsilon d$ ionization channels. The HF calculation for the $2p \to \epsilon d$ ionization channel is shown by the (green) open circles.

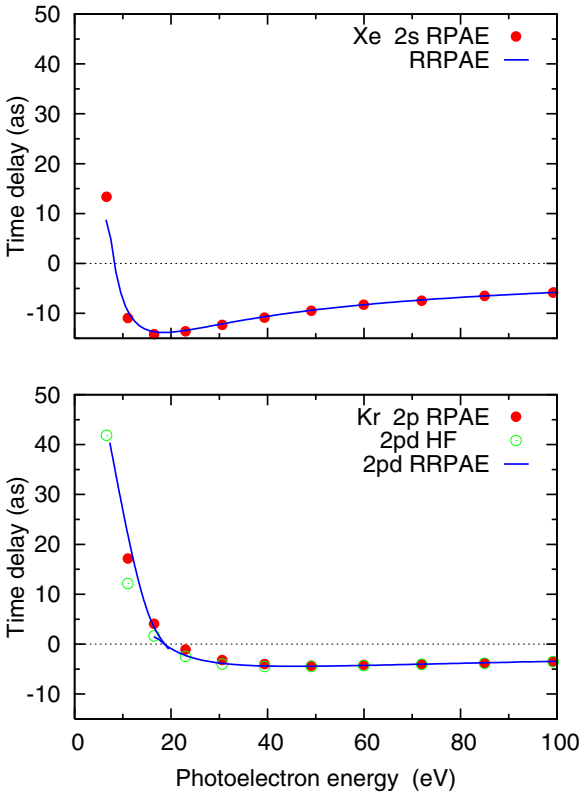

FIG. 7. (Color online) Time delay in photoionization of the $2s$ and $2p$ shells of Xe. Line styles are the same as those in Fig. 6.

IV. CONCLUSION

We conduct a systematic study of the dipole phase and the photoelectron group delay (Wigner time delay) in inner-shell photoionization of noble gas atoms from Ne to Xe. Our study encompasses the tender x-ray spectral range and extends to 1 keV photoelectron energy. We employ both the relativistic and the nonrelativistic versions of the random phase approximation with exchange. We identify the long-range Coulomb and the short-range Hartree-Fock contributions to the dipole phase which governs the Wigner time delay variation from the threshold to the whole range of photoelectron energies. Intershell correlations (interchannel coupling) are found to be significant in the $2s$ and $2p$ shells of Ne, the $3s$ subshell of Ar, and the $3d$ subshell of Kr. Relativistic effects do not significantly change the time delay results.

An interesting intershell correlation effect was reported recently [40] where an outer-shell photoionization cross section was influenced strongly by an inner shell near its threshold. We observed a strong modification of the time delay in such a situation and this was caused by exactly the same kind of interchannel coupling responsible for the structure reported in Ref. [40]. A more detailed report on this effect will be presented elsewhere.

We hope that our numerical results will serve as a useful benchmark in time-resolved studies of atomic ionization. Because the correlations do not play a determinative role in the photoionization of inner atomic shells, relatively simple HF or Dirac-Fock calculations may be sufficient for time delay evaluation that can be performed for a wide range of atoms with both closed and open shells. Because the inner shells are not strongly influenced by the chemical environment, similar time delays will be observed in corresponding inner shells of molecules and solids. Thus, it is expected that the phenomenology found for the photoionization time delay and the phases of the dipole amplitudes of noble gas atoms will be generally applicable to the qualitative behavior of inner shells in other atoms, both open- and closed-shell, molecules, and solids as well.

ACKNOWLEDGMENTS

The authors are very thankful to Valeriy Dolmatov for his critical reading of the manuscript and many useful comments. They also than Ishkhan Gorgisyan, Robert Moshammer, Thomas Pfeifer, and Jens Biegert for many stimulating discussions. A.K. acknowledges support by the Australian Research Council in the form of a Discovery Programme grant (Grant No. DP120101805). S.T.M. acknowledges the support of the Chemical Sciences, Geosciences and Biosciences Division, Office of Basic Energy Sciences, Office of Science, U.S. Department of Energy, under Grant No. DE-FG02-03ER15428. P.C.D. appreciates the support of a grant from the Department of Science and Technology, Government of India.

[1] H. Kleinpoppen, B. Lohmann, and A. Grum-Grzhimailo, *Perfect/Complete Scattering Experiments: Probing Quantum Mechanics on Atomic and Molecular Collisions and Coincidences*, Springer Series on Atomic, Optical, and Plasma Physics (Springer, Berlin, 2013).

[2] U. Heinzmann, Experimental determination of the phase differences of continuum wavefunctions describing the photoionisation process of xenon atoms, J. Phys. B **13**, 4367 (1980).

[3] N. A. Cherepkov and S. K. Semenov, On a complete experiment on photoionization of atoms, J. Phys. B **37**, 1267 (2004).

[4] J. Itatani, F. Quéré, G. L. Yudin, M. Y. Ivanov, F. Krausz, and P. B. Corkum, Attosecond Streak Camera, Phys. Rev. Lett. **88**, 173903 (2002).

[5] M. Schultze *et al.*, Delay in photoemission, Science **328**, 1658 (2010).

[6] L. Eisenbud, Formal properties of nuclear collisions, Ph.D. thesis, Princeton University, Princeton, NJ, 1948.

[7] E. P. Wigner, Lower limit for the energy derivative of the scattering phase shift, Phys. Rev. **98**, 145 (1955).

[8] F. T. Smith, Lifetime matrix in collision theory, Phys. Rev. **118**, 349 (1960).

[9] H. Muller, Reconstruction of attosecond harmonic beating by interference of two-photon transitions, Appl. Phys. B **74**, s17 (2002).

[10] K. Klünder, J. M. Dahlström, M. Gisselbrecht, T. Fordell, M. Swoboda, D. Guénot, P. Johnsson, J. Caillat, J. Mauritsson, A. Maquet, R. Taïeb, and A. L'Huillier, Probing Single-Photon Ionization on the Attosecond Time Scale, Phys. Rev. Lett. **106**, 143002 (2011).

[11] D. Guénot, K. Klünder, C. L. Arnold, D. Kroon, J. M. Dahlström, M. Miranda, T. Fordell, M. Gisselbrecht, P. Johnsson, J. Mauritsson, E. Lindroth, A. Maquet, R. Taïeb, A. L'Huillier, A. S. Mauritsson, and J. Kheifets, Photoemission-time-delay measurements and calculations close to the 3*s*-ionization-cross-section minimum in Ar, Phys. Rev. A **85**, 053424 (2012).

[12] S. B. Schoun, R. Chirla, J. Wheeler, C. Roedig, P. Agostini, L. F. DiMauro, K. J. Schafer, and M. B. Gaarde, Attosecond Pulse Shaping Around a Cooper Minimum, Phys. Rev. Lett. **112**, 153001 (2014).

[13] M. Negro, D. Faccialá, B. Bruner, M. Devetta, S. D. Silvestri, N. Dudovich, S. Pabst, R. Santra, H. Soifer, S. Stagira *et al.*, Probing Xenon Electronic Structure by Two-Color Driven High-Order Harmonic Generation, in *Ultrafast Phenomena XIX*, Proceedings in Physics Vol. 162 (Springer, New York, 2015), pp. 7–10.

[14] T. Popmintchev, M.-C. Chen, P. Arpin, M. M. Murnane, and H. C. Kapteyn, The attosecond nonlinear optics of bright coherent x-ray generation, Nat. Photonics **4**, 822 (2010).

[15] B. Wolter, M. G. Pullen, M. Baudisch, M. Sclafani, M. Hemmer, A. Senftleben, C. D. Schröter, J. Ullrich, R. Moshammer, and J. Biegert, Strong-Field Physics with Mid-IR Fields, Phys. Rev. X **5**, 021034 (2015).

[16] J. Biegert (private communication, 2015).

[17] G. Schmid, XUV-pump THz-probe experiments on neon at the free-electron laser in Hamburg, Master's thesis, Ruprecht-Karls-Universität, Heidelberg, 2013, http://hdl.handle.net/11858/00-001M-0000-0014-9DBB-7.

[18] G. Schmid *et al.*, Terahertz field induced time shifts in atomic photoemission, Phys. Rev. Lett. (to be published).

[19] U. Fruhling, M. Wieland, M. Gensch, T. Gebert, B. Schutte, M. Krikunova, R. Kalms, F. Budzyn, O. Grimm, J. Rossbach *et al.*, Single-shot terahertz-field-driven x-ray streak camera, Nat. Photonics **3**, 523 (2009).

[20] I. Grguras, A. R. Maier, C. Behrens, T. Mazza, T. J. Kelly, P. Radcliffe, S. Dusterer, A. K. Kazansky, N. M. Kabachnik, T. Tschentscher *et al.*, Ultrafast x-ray pulse characterization at free-electron lasers, Nat. Photonics **6**, 852 (2012).

[21] P. N. Juranić, A. Stepanov, R. Ischebeck, V. Schlott, C. Pradervand, L. Patthey, M. Radović, I. Gorgisyan, L. Rivkin, C. P. Hauri *et al.*, High-precision x-ray FEL pulse arrival time measurements at SACLA by a THz streak camera with Xe clusters, Opt. Express **22**, 30004 (2014).

[22] I. Gorgisyan, R. Ischebeck, E. P. Costa, S. Reiche, L. Rivkin, and P. Juranic, Simulation of fel pulse length calculation with THz streaking method, J. Synchr. Rad. (to be published).

[23] A. C. Thompson, D. T. Attwood, E. M. Gullikson, M. R. Howells, J. B. Kortright, A. L. Robinson, and J. H. Underwood, *X-Ray Data Booklet* (Center for X-ray Optics and Advanced Light Source, Lawrence Berkeley National Laboratory, 2009).

[24] A. S. Kheifets, Time delay in valence-shell photoionization of noble-gas atoms, Phys. Rev. A **87**, 063404 (2013).
[25] S. Saha, A. Mandal, J. Jose, H. R. Varma, P. C. Deshmukh, A. S. Kheifets, V. K. Dolmatov, and S. T. Manson, Relativistic effects in photoionization time delay near the Cooper minimum of noble-gas atoms, Phys. Rev. A **90**, 053406 (2014).
[26] J. Berkowitz, *Photoabsorption, Photoionization, and Photoelectron Spectroscopy* (Elsevier, Amsterdam, 2012).
[27] I. Band, Y. Kharitonov, and M. Trzhaskovskaya, Photoionization cross sections and photoelectron angular distributions for x-ray line energies in the range 0.132–509 keV targets: $1 \leqslant Z \leqslant 100$, At. Data Nucl. Data Tables **23**, 443 (1979).
[28] R. Pazourek, S. Nagele, and J. Burgdorfer, Time-resolved photoemission on the attosecond scale: Opportunities and challenges, Faraday Discuss. **163**, 353 (2013).
[29] J. Dahlström, D. Guénot, K. Klünder, M. Gisselbrecht, J. Mauritsson, A. L'Huillier, A. Maquet, and R. Taïeb, Theory of attosecond delays in laser-assisted photoionization, Chem. Phys. **414**, 53 (2012).
[30] L. V. Chernysheva, N. A. Cherepkov, and V. Radojevic, Self-consistent field Hartree-Fock program for atoms, Comput. Phys. Commun. **11**, 57 (1976).
[31] L. V. Chernysheva, N. A. Cherepkov, and V. Radojevic, Frozen core Hartree-Fock program for atomic discrete and continuous states, Comput. Phys. Commun. **18**, 87 (1979).
[32] W. R. Johnson and C. D. Lin, Multichannel relativistic random-phase approximation for the photoionization of atoms, Phys. Rev. A **20**, 964 (1979).
[33] U. Fano, Propensity rules: An analytical approach, Phys. Rev. A **32**, 617 (1985).
[34] J. C. A. Barata, L. F. Canto, and M. S. Hussein, New asymptotic formulas for the point Coulomb phase shift, Braz. J. Phys. **41**, 50 (2011).
[35] L. Rosenberg, Levinson-Seaton theorem for potentials with an attractive Coulomb tail, Phys. Rev. A **52**, 3824 (1995).
[36] D. J. Kennedy and S. T. Manson, Photoionization of the noble gases: Cross sections and angular distributions, Phys. Rev. A **5**, 227 (1972).
[37] S. T. Manson, Dependence of the phase shift on energy and atomic number for electron scattering by atomic fields, Phys. Rev. **182**, 97 (1969).
[38] V. V. Serov, V. L. Derbov, and T. A. Sergeeva, Interpretation of time delay in the ionization of two-center systems, Phys. Rev. A **87**, 063414 (2013).
[39] M. Ivanov and O. Smirnova, How Accurate is the Attosecond Streak Camera?, Phys. Rev. Lett. **107**, 213605 (2011).
[40] W. Drube, T. M. Grehk, S. Thieß, G. B. Pradhan, H. R. Varma, P. C. Deshmukh, and S. T. Manson, Pronounced effects of interchannel coupling in high-energy photoionization, J. Phys. B **46**, 245006 (2013).